Society of Medical Education & Research

2021, Volume 1, Page No: 150-170

ISSN: 3108-4834

Archive of International Journal of Cancer and Allied Science

STC1–Neutrophil Extracellular Trap Positive Feedback Loop Drives Immune Escape and Metastasis in Bladder Cancer

Sarah Louise Bennett[1]*, Claire Marie Thompson[1]

[1]Department of Cancer Sciences, University of Manchester, Manchester, United Kingdom.

***E-mail** ✉ s.bennett.cancer@yahoo.com

Abstract

Despite the clinical success of immune checkpoint inhibitors (ICIs) in bladder cancer (BLCA), many patients fail to respond due to primary resistance. Neutrophil extracellular traps (NETs) have recently emerged as critical mediators of tumor therapy resistance, yet their precise function in BLCA is still unclear. We combined data from multiple ICI-treated patient cohorts to investigate the association between NET levels and clinical outcomes. Experimental approaches—including immunofluorescence, in vitro co-culture, scanning electron microscopy, and a mouse lung metastasis model—were employed to examine NETs' biological impact. Molecular mechanisms were further explored using proteomic profiling and single-cell transcriptomics.

BLCA samples exhibited abnormal NET accumulation, which enhanced metastasis and reduced ICI effectiveness in mice. Mechanistic studies demonstrated that NETs stimulate STC1 expression in tumor cells through the TLR2-MAPK-FosL1 pathway. STC1 restrained antigen presentation by capturing calreticulin, while its secreted form promoted further NET formation, creating a self-amplifying feedback loop. Additionally, secreted STC1 hindered CD14+ precursors from differentiating into mature dendritic cells, intensifying immunosuppression. These findings reveal a key immunosuppressive NETs-STC1 circuit in BLCA, suggesting that targeting this pathway could improve both therapeutic efficacy and safety of ICIs.

Keywords: Bladder cancer, Neutrophil, Immunotherapy, Immune-related adverse event - irAE

Introduction

Muscle-invasive bladder cancer (MIBC) represents roughly one-quarter of new BLCA diagnoses and is highly aggressive. Once distant metastases develop, the 5-year survival rate falls to 5–15%, making effective treatment particularly difficult [1, 2]. While ICIs have substantially improved outcomes in advanced BLCA, only a minority of patients achieve lasting responses, with durable benefit observed in fewer than 25% [3, 4]. Immune-related adverse events (irAEs) frequently compromise treatment continuity and long-term efficacy [5, 6]. For example, the 2023 KEYNOTE-045 trial reported an objective response rate of just 21.1% for anti-PD-1 therapy, with 16.5% of patients experiencing grade ≥3 irAEs [7]. Existing biomarkers, including PD-L1 expression and tumor mutational burden, lack sufficient predictive power [8], highlighting an urgent need for novel biomarkers and combination strategies.

The limited efficacy of ICIs is heavily influenced by the immunosuppressive tumor microenvironment (TME) [9]. BLCA exhibits significant immune heterogeneity, and tumor cells employ diverse mechanisms to evade immune surveillance [10], including defects in antigen presentation [11], elevated secretion of immunosuppressive factors [12], and poor infiltration of effector T cells [13]. The role of non-lymphocyte immune cells, particularly neutrophils, in shaping tumor immunity is increasingly recognized [14–16].

Tumor-associated neutrophils (TANs) are major TME constituents that promote tumor growth and dissemination via multiple mechanisms [17]. Clinically, a high neutrophil-to-lymphocyte ratio (NLR) is

Access this article online https://smerpub.com/

Received: 28 May 2021; **Accepted:** 12 October 2021

How to cite this article: Bennett SL, Thompson CM. STC1–Neutrophil Extracellular Trap Positive Feedback Loop Drives Immune Escape and Metastasis in Bladder Cancer. Arch Int J Cancer Allied Sci. 2021;1:150-70. https://doi.org/10.51847/89R10Bxc2B

associated with immunotherapy resistance and worse patient outcomes [18]. TANs facilitate metastasis partly through the release of NETs, which are DNA-protein networks originally characterized for pathogen defense [19, 20]. Within the TME, NETs can accumulate abnormally under various stimuli [21], promoting epithelial-mesenchymal transition (EMT) or forming physical barriers around tumor cells, thus shielding them from immune attack [22].

Although NETs' role in tumor progression and metastasis is recognized, their contribution to immune evasion and ICI resistance in BLCA remains poorly defined. Whether NETs act as immunosuppressive mediators in the TME and influence immunotherapy outcomes has yet to be elucidated.

In this study, we integrated clinical data from multiple ICI-treated cohorts, analyzed patient samples, and used preclinical models to clarify NETs' role in BLCA metastasis and immunotherapy resistance, aiming to identify combination strategies targeting NETs to enhance both the efficacy and safety of ICIs.

Materials and Methods

Clinical specimen acquisition

Specimens were gathered from September 2022 through March 2025 at two institutions: Fudan University Shanghai Cancer Center (FUSCC) and Sun Yat-sen University Cancer Center (SYSUCC). Blood samples were drawn from the peripheral circulation of patients diagnosed with bladder urothelial carcinoma (BLCA) as well as from healthy volunteers (HDs). Surgical resections provided paired tumor and nearby non-cancerous tissue samples from BLCA cases undergoing either transurethral bladder tumor resection or complete cystectomy. Importantly, all patients were treatment-naïve at enrollment, having received no prior chemotherapy, radiation, immune-based therapy, or any other anticancer interventions before their operations.

Maintenance of cell lines

Human bladder cancer cell lines UMUC-3 (CVCL_1783), 5637 (CVCL_0126), and T24 (CVCL_0554), the mouse bladder cancer line MB49 (CVCL_7076), and the human embryonic kidney line HEK293T (CVCL_0063) were procured from the China Center for Type Culture Collection. Cells were grown in Dulbecco's Modified Eagle Medium (HyClone) supplemented with 10% fetal bovine serum plus 1% penicillin/streptomycin mixture. Incubation occurred at 37°C in a 5% CO_2 humidified environment. Routine screening confirmed the absence of Mycoplasma contamination in all lines.

Establishment of STC1-deficient cell models

An STC1-null MB49 line was created using CRISPR/Cas9 technology. A guide RNA specific to the murine Stc1 locus was complexed with Cas9 and delivered to MB49 cells. Successful gene disruption was assessed via western blotting, qPCR, and ELISA. Several validated clonal populations (sgSTC1#1, #2, and #3) were combined for later studies.

In the human 5637 line, stable STC1 silencing was achieved through lentiviral delivery of short hairpin RNAs (shSTC1#1, #2, #3) or a scrambled control (shNC). Infection was enhanced with 2 μg/mL polybrene (Sigma-Aldrich), followed by antibiotic selection beginning 48 hours later. Reduction of STC1 expression was confirmed by western blot, qPCR, and ELISA.

Neutrophil purification and induction of neutrophil extracellular traps (NETs)

Fifteen milliliters of peripheral blood were obtained from healthy volunteers. Neutrophils were separated using a commercial Human Neutrophil Isolation Kit (LZS11131, TBD Science) per the supplied protocol. Blood was carefully overlaid on a ficoll-based gradient and spun at 600 × g for 35 minutes. The enriched neutrophil fraction was collected, washed twice in sterile PBS (350 × g, 10 minutes each), and finally resuspended in RPMI-1640 before a 1-hour recovery period at 37°C with 5% CO_2.

To generate NETs, 1×10^7 freshly purified neutrophils per well were plated in six-well dishes and treated with 500 nM PMA (P1585, Sigma-Aldrich) for 4 hours under standard culture conditions. Released NET structures and suspended cells were then harvested by gentle scraping, followed by three rinses with chilled RPMI-1640. Cellular debris was pelleted by centrifugation (350 × g, 10 minutes). The resulting cell-free supernatant, designated NET-conditioned medium (NETs-CM), was measured for double-stranded DNA content with the Qubit HS Assay Kit (Q32851, Invitrogen) on a Qubit 4.0 instrument. Standardized stocks (1,000 ng DNA/mL) were cryopreserved at −80°C and thawed with a 1:10 dilution before use. Where indicated, NETs were dismantled by adding DNase I (150 U/mL; LS006322, Worthington).

Purification of CD14⁺ monocytes and establishment of co-culture

PBMCs were isolated from healthy donor blood via density gradient separation using Human Lymphocyte Separation Medium (DKW-KLSH-0100; Dakewei). From these, $CD14^+$ monocytes were positively selected with CD14 MicroBeads (130-118-906, Miltenyi Biotec), yielding populations with greater than 95% purity as assessed by flow cytometry.

For indirect co-culture, 5637 cells harboring either STC1-specific shRNA (shSTC1#3) or scrambled control (shNC) were seeded at 2×10^5 cells per well into the lower compartment of 24-well Transwell inserts (0.4 μm pores; 3412, Corning) and cultured overnight for attachment. Freshly prepared $CD14^+$ monocytes were then introduced at 1×10^6 cells per insert into the upper compartment. The system was incubated for 48 hours under standard conditions (37°C, 5% CO_2, humidified).

Visualization of NETs by scanning electron microscopy

To induce NET formation, neutrophils were treated with tumor cell-derived conditioned medium; resting neutrophils served as negative controls, while PMA-activated cells acted as positive controls. Fixed samples were preserved in 2.5% glutaraldehyde (in 0.1 M phosphate buffer) overnight at 4°C to maintain integrity of extracellular DNA-protein lattices. A stepwise ethanol dehydration protocol was applied to avoid distortion of fine NET threads. High-resolution imaging was performed on an APREO 2 SEM instrument (Thermo Fisher). Areas displaying NETs were characterized by mesh-like networks larger than 5 μm across, featuring crossed fibrous DNA elements.

Western blot analysis

Lysis was carried out in RIPA buffer (89901, Thermo Scientific) fortified with protease/phosphatase inhibitor cocktail (78440, Thermo Fisher). Total protein was measured using BCA assay (A55860, Thermo Fisher). Primary antibodies, diluted as follows, were probed overnight at 4°C under rotation: anti-citrullinated histone H3 (1:1,000; ab281584, Abcam); anti-STC1 (1:1,000; sc-293435, Santa Cruz); anti-calreticulin (CRT) (1:3,000; 27298–1-AP, Proteintech); anti-FosL1 (1:1,000; 5281, CST); anti-MEK1/2 (1:1,000; 9122, CST); anti-phospho-MEK1/2 (1:1,000; 9154, CST); anti-ERK1/2 (1:1,000; 4695, CST); anti-phospho-ERK1/2 (1:1,000; 5726, CST); anti-ATP1A1 (1:5,000; 55187–1-AP, Proteintech); anti-GAPDH (1:10,000; 60004–1-Ig, Proteintech); anti-Histone H3 (1:5,000; 17168–1-AP, Proteintech); anti-α-tubulin (1:5,000; Proteintech); anti-Flag (1:1,000; 2368S, CST). Corresponding secondary antibodies were added for 2 hours at ambient temperature.

Chromatin immunoprecipitation followed by qPCR (ChIP-qPCR)

FosL1 occupancy on the STC1 promoter was examined using the ChIP Assay Kit (17–10086, Millipore) per manufacturer guidelines. UMUC-3 cells underwent crosslinking with 1% formaldehyde (10 minutes), terminated by glycine addition. Following PBS rinsing, nuclear lysates were sonicated to yield DNA fragments ranging 200–500 bp. Immunoprecipitation involved overnight incubation with anti-FosL1 (5281, CST) or isotype-matched IgG, followed by capture on protein A/G beads. Washed complexes were decrosslinked via heating with proteinase K, and purified DNA served as template for qPCR amplification of STC1 promoter sequences.

Co-immunoprecipitation (Co-IP)

Both HEK293T and UMUC-3 cells were harvested in chilled RIPA buffer containing inhibitor cocktails and lysed for 30 minutes on ice. Debris was removed by high-speed centrifugation (12,000 × g, 30 minutes, 4°C). For reciprocal pulldowns, 500 μg protein was rotated overnight at 4°C with 2 μg anti-STC1 (sc-293435, Santa Cruz) or anti-CRT (27298–1-AP, Proteintech). Resolved proteins (10% gels, PVDF transfer) from inputs (10%) and eluates were detected using the counterpart antibody: anti-CRT (1:3,000) for STC1 IPs or anti-STC1 (1:1,000) for CRT IPs.

Immunofluorescence assays

NET detection in clinical BLCA samples used 5 μm paraffin sections subjected to deparaffinization, rehydration, and heat-mediated antigen retrieval in Tris/EDTA. Permeabilization (0.2% Triton X-100) preceded blocking (5% BSA). Overnight primary incubation at 4°C employed anti-citrullinated histone H3 (citH3; 1:500) and anti-myeloperoxidase (MPO; 1:1,000). Fluorescent secondaries (Alexa Fluor 488/555; 1:5,000; A11029/A21429, Invitrogen) were applied for 2 hours before DAPI counterstain. Confocal imaging (Olympus FV3000) captured citH3+/MPO+/DAPI+ overlapping signals indicative of NETs. ImageJ (v1.53) quantification involved line scans across tumor regions,

generation of citH3 intensity plots, and computation of area under the curve (AUC; AU × pixels).

STC1-CRT interaction studies in UMUC-3 cells included mitochondrial staining with Mito-Tracker Deep Red (100 nM, 30 minutes; C1034, Beyotime) prior to 4% paraformaldehyde fixation and permeabilization. Blocked cells (1% BSA) received overnight anti-STC1 (1:100; sc-293435, Santa Cruz) and anti-CRT (1:100; 27298–1-AP, Proteintech). Secondary labeling (Alexa Fluor 488/555; 1:5,000) and DAPI (1 µg/mL) followed. Confocal acquisition (Olympus FV3000) and colocalization (FIJI Coloc2; Pearson's $r > 0.5$ denoting interaction) completed the analysis.

Quantitative spatial proximity analysis

Spatial relationships between neutrophil extracellular traps (NETs) and T cells in mouse lung metastatic tissues were quantified using HALO software (V.4.0, Indica Labs) with the Highplex FL module. The analysis measured the presence of citH3+ cells within defined radii around CD4+ and CD8+ T cells to determine whether NETs and T cells exhibited spatial exclusion patterns. Counts of different cell types were recorded across distance intervals to map their relative distributions.

Lung metastasis model and experimental treatments

Six-week-old C57BL/6 mice were injected intravenously with 1×10^5 MB49-Luc cells suspended in 200 µL PBS via the tail vein. Metastatic burden was monitored weekly for four weeks using bioluminescent imaging (IVIS Spectrum, PerkinElmer), and body weight was tracked twice weekly as a general health metric. To modulate NET levels, mice received a tail vein injection of lipopolysaccharide (LPS; 10 µg/mouse; L2880, Sigma-Aldrich) 24 hours before tumor cell inoculation. In selected groups, DNase I (300 U/mouse; LS006322, Worthington) was administered intraperitoneally to degrade NETs. Immune checkpoint blockade was performed with intraperitoneal injections of InVivoMAb anti-mouse PD-1 (200 µg/mouse; BE0146, Bio X Cell) or IgG control three times per week. For in vivo depletion experiments, mice were treated with InVivoMAb antibodies targeting CD8α, CSF1R, or NK1.1 (or their matched IgG controls) starting three days prior to tumor inoculation, followed by repeated dosing of 400 µg every three days throughout tumor progression [23].

Single-cell RNA sequencing analysis

Publicly available single-cell RNA sequencing (scRNA-seq) data associated with immune-related adverse events (irAEs) were obtained from the Gene Expression Omnibus (GEO, GSE180045) [24]. Patients were classified into two groups: those receiving immune checkpoint inhibitor (ICI) therapy without irAEs (A1, A2, A3) and those who developed irAEs after ICI treatment (B1, B2, B3, MCE1, MCE2, MCL1, MCL3). Data processing was carried out in R using the Seurat package (V.4.4.1). Doublets were identified and removed with DoubletFinder, and low-quality cells were filtered out if they had fewer than 200 or more than 6,000 detected genes or mitochondrial gene content exceeding 20%. Genes expressed in fewer than five cells were excluded. Cell cycle scores were computed with CellCycleScoring(), and the effects of the cell cycle were regressed out via the regress.out parameter in ScaleData(). Following normalization and scaling, batch effects were corrected using Harmony, and the top 3,000 variable genes were selected. Principal component analysis (PCA) was performed using the top 2,000 highly variable genes, with the first 15 principal components applied to generate UMAP embeddings. Clustering was performed with FindClusters() at a resolution of 0.5, and cell types were annotated based on classical literature markers in combination with cluster-specific characteristics [24]. Data visualization was generated using the omicverse Python module.

MCP-counter deconvolution and pathway analysis

The MCP-counter algorithm was employed to quantify immune cell populations in transcriptomic datasets, allowing absolute abundance estimation [25]. To investigate myeloid cell heterogeneity, CD14+ cells extracted from the MCP-counter results underwent deconvolution analysis, highlighting differences in cell composition between experimental groups. Additionally, single-sample Gene Set Enrichment Analysis (ssGSEA) was applied to predefined immune pathways to uncover distinct immune signatures [26]. Complementary Gene Set Enrichment Analysis (GSEA) based on the Gene Ontology (GO) database provided a broader assessment of biological processes associated with the observed transcriptional patterns.

Statistical analysis

Analyses were performed using GraphPad Prism (V.10.0), R (V.4.2.4), and Python (V.3.9). Normally distributed continuous variables were evaluated using a

two-tailed Student's t-test for pairwise comparisons or one-way ANOVA for comparisons involving three or more groups. Non-parametric data were analyzed using the Wilcoxon rank-sum test (two groups) or the Kruskal-Wallis test (three or more groups). Experiments with factorial designs were assessed by two-way ANOVA. Kaplan-Meier curves were generated for survival analysis, with differences assessed via the log-rank test. Correlations were quantified using Pearson's coefficient for linear relationships or Spearman's rank for non-linear relationships. Categorical variables were compared with χ^2 or Fisher's exact test. All experiments included at least three independent biological replicates. Data are presented as mean ± SD for parametric data or median with interquartile range for non-parametric data, following STRIVE guidelines. Statistical significance was defined as $p<0.05$ (two-tailed), and exact p-values are reported for key analyses. Significance is indicated as: ns, not significant; *p<0.05, **p<0.01, ***p<0.001, ****p<0.0001.

Results and Discussion

NET accumulation is linked to BLCA progression and immunotherapy failure

To explore the impact of neutrophil extracellular traps (NETs) on bladder cancer (BLCA) progression and response to immunotherapy, citH3 and MPO were measured in tumor tissues from two independent patient cohorts. Areas showing overlap between citH3 and MPO were defined as NET-positive [27]. Immunofluorescence imaging revealed stronger co-localization of citH3 and MPO in tumors from immunotherapy non-responders compared with responders in the FUSCC cohort **(Figures 1a and 1b)**. Line-scan analysis across tumor sections demonstrated higher citH3 signal intensity and a significantly larger area under the curve (AUC) in non-responders **(Figures 1c and 1d)**. CitH3 serves as the most specific marker for NETs [21]. Immunohistochemistry of tumors (FUSCC cohort, n=27) confirmed that citH3-positive areas were more extensive in non-responders **(Figure 1e)**, a finding further supported by western blot showing elevated citH3 protein levels. Serum MPO-DNA complexes, indicative of systemic NET burden [28], were also higher in non-responders across both cohorts **(Figures 1f and 1j)**. Subgroup analyses revealed that increased NET load—measured either by tumor citH3 or serum MPO-DNA—was associated with poor immunotherapy response **(Figures 1g and 1i)**, enhanced metastatic potential **(Figures 1h and 1i)**, and shorter progression-free survival **(Figure 1k)**.

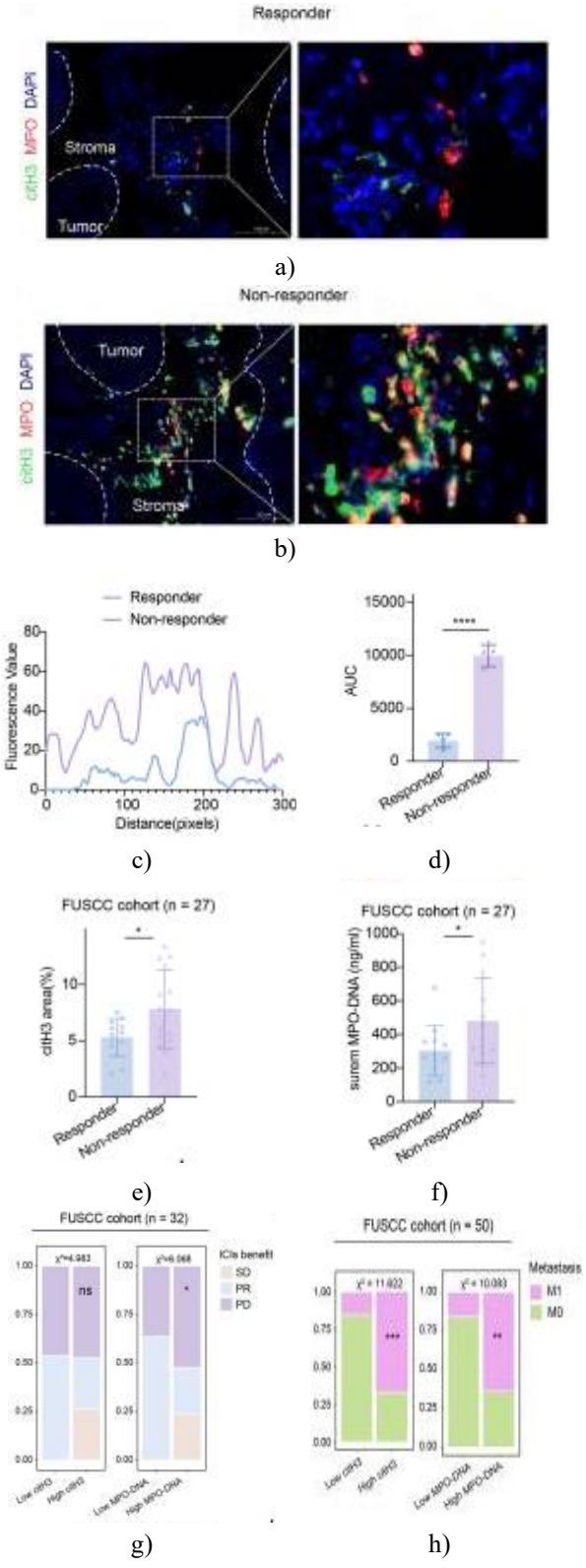

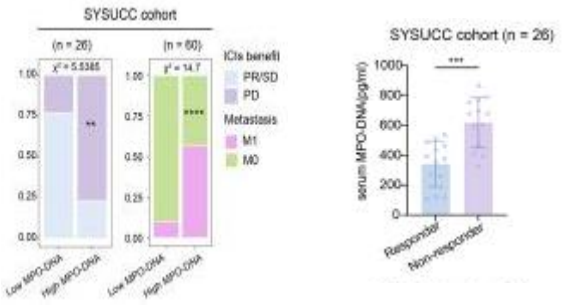

i) j)

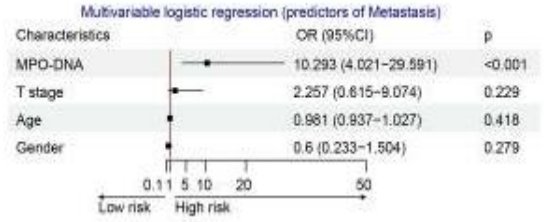

l)

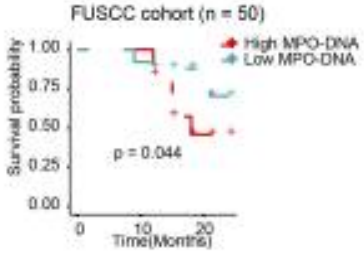

k)

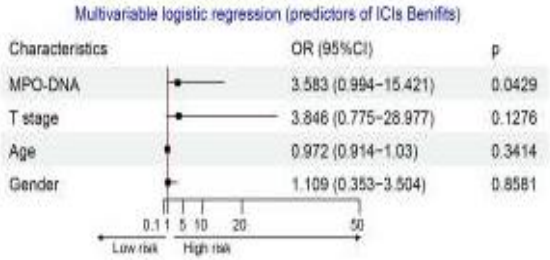

m)

Figure 1. NET Levels Correlate with Tumor Progression and Immunotherapy Resistance in BLCA. Panels a–b display representative immunofluorescence (IF) images highlighting co-localization of NET markers citH3 (green) and MPO (red) in BLCA tissues from patients responding (a) or not responding (b) to immunotherapy. Line-scan analysis of citH3 fluorescence across tumor sections (c) indicated higher signal intensity along the scan distance in non-responders (purple) compared with responders (blue), with quantification by area under the curve (AUC) confirming a significantly elevated fluorescence in non-responders (d). Tumor citH3 expression (e) and serum MPO-DNA complex levels (f) were higher in non-responders in the FUSCC cohort (n=27). When patients were stratified by high versus low citH3 or MPO-DNA, objective response rate (ORR) to immunotherapy was reduced in the high NET group (g, n=32). Furthermore, higher tumor citH3 and serum MPO-DNA were associated with metastatic disease (h, n=50), and these findings were validated in the SYSUCC cohort for both metastasis (i, n=60) and immunotherapy response (j, n=26). Kaplan-Meier analysis showed shorter progression-free survival (PFS) in patients with elevated serum MPO-DNA (k). Multivariable logistic regression accounting for tumor T stage, age, and gender confirmed circulating MPO-DNA as an independent predictor of metastasis (l) and reduced ICIs benefit (m). Abbreviations: AU= arbitrary units; AUC= area under the curve; BLCA= bladder cancer; FUSCC, Fudan University Shanghai Cancer Center; ICI= immune checkpoint inhibitor; IF= immunofluorescence; MPO, myeloperoxidase; NETs= neutrophil extracellular traps; ORR= objective response rate; PFS= progression-free survival; PD= progressive disease; PR= partial response; SD= stable disease; SYSUCC= Sun Yat-sen University Cancer Center.

Multivariable logistic regression revealed that serum MPO-DNA independently predicted metastasis (OR 10.293, 95 percent CI 4.021–29.591; p<0.001) and reduced immunotherapy benefit (OR 3.583, 95 percent CI 0.994–15.421; p=0.0429), while other covariates had no significant effect **(Figures 1l and 1m)**. Overall, these findings indicate that NET abundance is positively associated with metastatic progression and poor immunotherapy response in BLCA, suggesting that NETs may act not only as biomarkers but as active mediators of immune evasion and tumor spread.

NETs promote experimental metastasis via immune-dependent mechanisms and shape an immunosuppressive tumor microenvironment

To directly assess the contribution of NETs to metastasis and immune resistance, a lung metastasis model with high NET induction was established using LPS in C57BL/6 and nude mice **(Figure 2a)**. NET induction was validated by monitoring serum MPO-DNA. In vivo bioluminescence imaging demonstrated that LPS-

induced NETs enhanced metastasis in immunocompetent C57BL/6 mice, whereas metastasis was not significantly increased in immunodeficient nude mice. DNase I treatment reduced metastatic burden in C57BL/6 mice but had a diminished effect in nude mice **(Figures 2b and 2c)**. Histological assessment confirmed larger metastatic lesions in the lungs of C57BL/6 mice treated with LPS.

To clarify whether NET-mediated metastasis was dependent on antitumor immunity, antibody-mediated depletion of CD8+ T cells or NK1.1+ cells was performed in C57BL/6 mice. DNase I significantly reduced metastasis in IgG and NK1.1-depleted mice but failed to do so when CD8+ T cells were depleted **(Figures 2d and 2e)**, indicating that NETs exert pro-metastatic effects largely through suppression of CD8+ T-cell–mediated immunity. Flow cytometry of lung lesions showed that LPS increased neutrophil infiltration while reducing both the abundance and functional capacity of CD8+ T cells, as indicated by lower expression of TCF1 (stem-like), granzyme B (cytotoxicity), and CD107a (degranulation) **(Figures 2f and 2h)**. Spatial mapping revealed that LPS decreased intratumoral densities of CD4+ and CD8+ T cells, whereas DNase I restored T-cell localization within tumor parenchyma **(Figures 2i and 2j)**. Distance-to-centroid analyses further demonstrated that CD4+/CD8+ T cells were displaced farther from tumor cores in the LPS group, and DNase I partially reversed this effect **(Figure 2k)**. Collectively, these findings demonstrate that NETs promote metastasis through immune-dependent mechanisms and contribute to the establishment of an immunosuppressive tumor microenvironment.

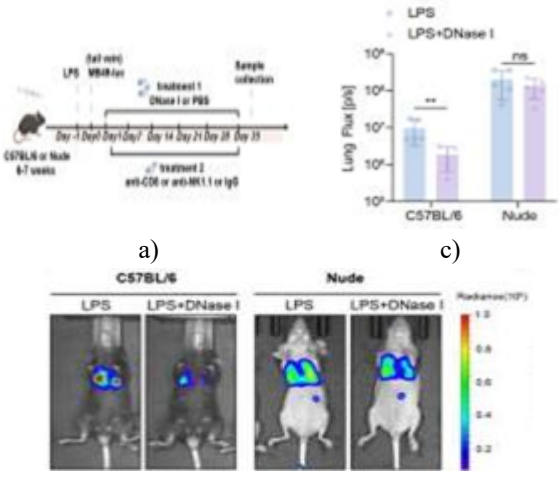

a) c) b)

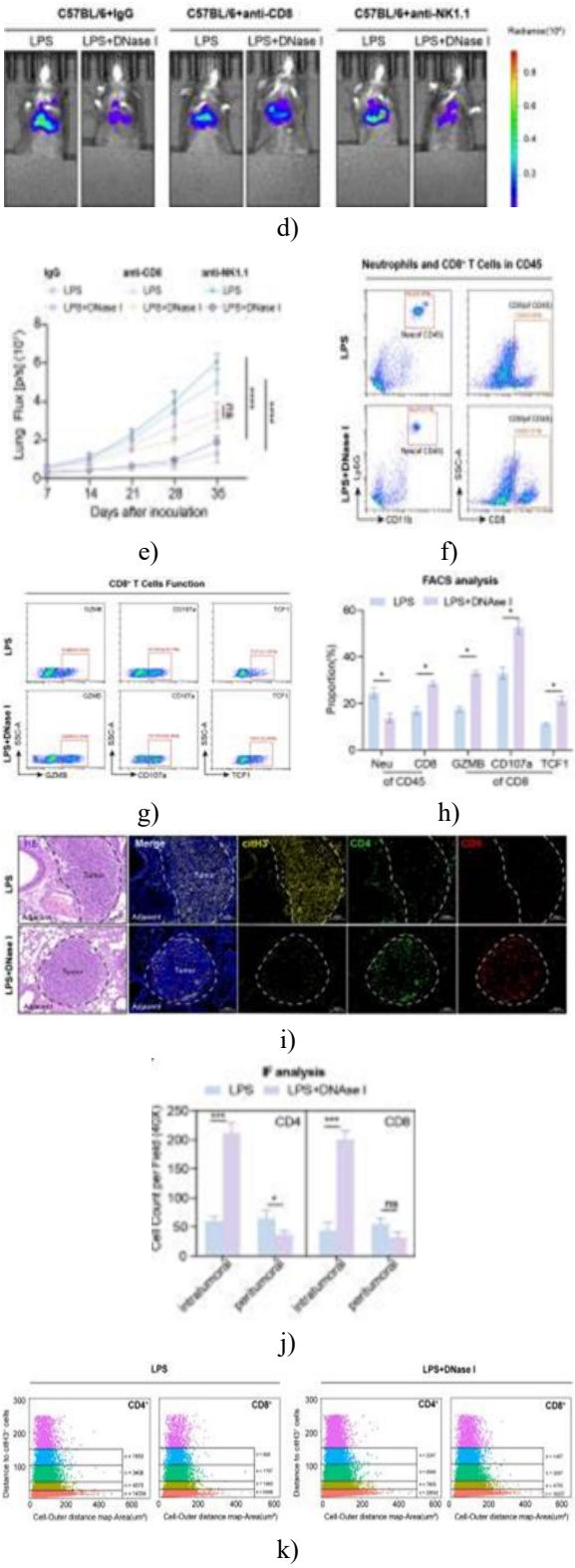

d) e) f) g) h) i) j) k)

Figure 2. NETs Promote Experimental Metastasis via Immune-Dependent Mechanisms and Establish an Immunosuppressive TME. (a) Schematic overview of the lung metastasis experimental setup.

MB49-luc cells were administered via tail vein injection, NET formation was induced with LPS, and NETs were disrupted using DNase I. Where indicated, mice received IgG control, anti-CD8, or anti-NK1.1 antibodies according to the timeline shown. (b–c) Representative bioluminescence images (b) and quantitative analysis (c) of metastatic tumor burden in both C57BL/6 and nude mice under LPS or LPS+DNase I treatment conditions. LPS enhanced metastatic spread in immunocompetent mice, while DNase I mitigated this effect; in immunodeficient nude mice, metastasis was largely unaffected. (d–e) Bioluminescence imaging (d) and lung radiance quantification (e) across cohorts depleted of CD8+ T cells, NK1.1+ cells, or receiving IgG control, each under LPS or LPS+DNase I treatment. DNase I reduced metastatic burden in IgG and NK1.1-depleted mice, but not in CD8+ T-cell–depleted mice, indicating the pro-metastatic effect of NETs is largely dependent on CD8+ T-cell–mediated immunity. (f–h) Flow cytometry analyses show neutrophil and CD8+ T-cell infiltration (f), functional marker expression (TCF1, GZMB, CD107a) (g), and quantitative assessment (h) in lung metastatic foci from C57BL/6 mice. LPS increased neutrophil presence while diminishing both the number and functional activity of CD8+ T cells. (i) Representative H&E and IF co-staining images (citH3, CD4, CD8) of lung metastatic lesions from C57BL/6 mice. (j–k) Spatial analyses of tumor-infiltrating lymphocytes demonstrate that NETs restrict intratumoral accumulation of CD4+ and CD8+ T cells compared with peritumoral regions, quantified by cell counts per field (j) and distance-to-tumor-centroid measurements (k).

Combination of anti-PD-1 and NET inhibition improves therapeutic outcomes in BLCA

Based on the observed immunosuppressive effects of NETs, we investigated whether targeting NETs could enhance immunotherapy efficacy. In the LPS-induced high-NETs lung metastasis model, mice were assigned to four treatment groups: isotype control, DNase I alone, anti-PD-1 alone, and the combination of anti-PD-1 with DNase I **(Figure 3a)**. In vivo bioluminescence imaging revealed that the combination therapy markedly reduced metastatic burden compared with anti-PD-1 monotherapy, with statistically significant differences **(Figures 3b and 3c)**. Histopathological evaluation corroborated these findings, showing a clear decrease in lung metastatic foci in the combination group relative to the anti-PD-1 alone group **(Figures 3d and 3e)**.

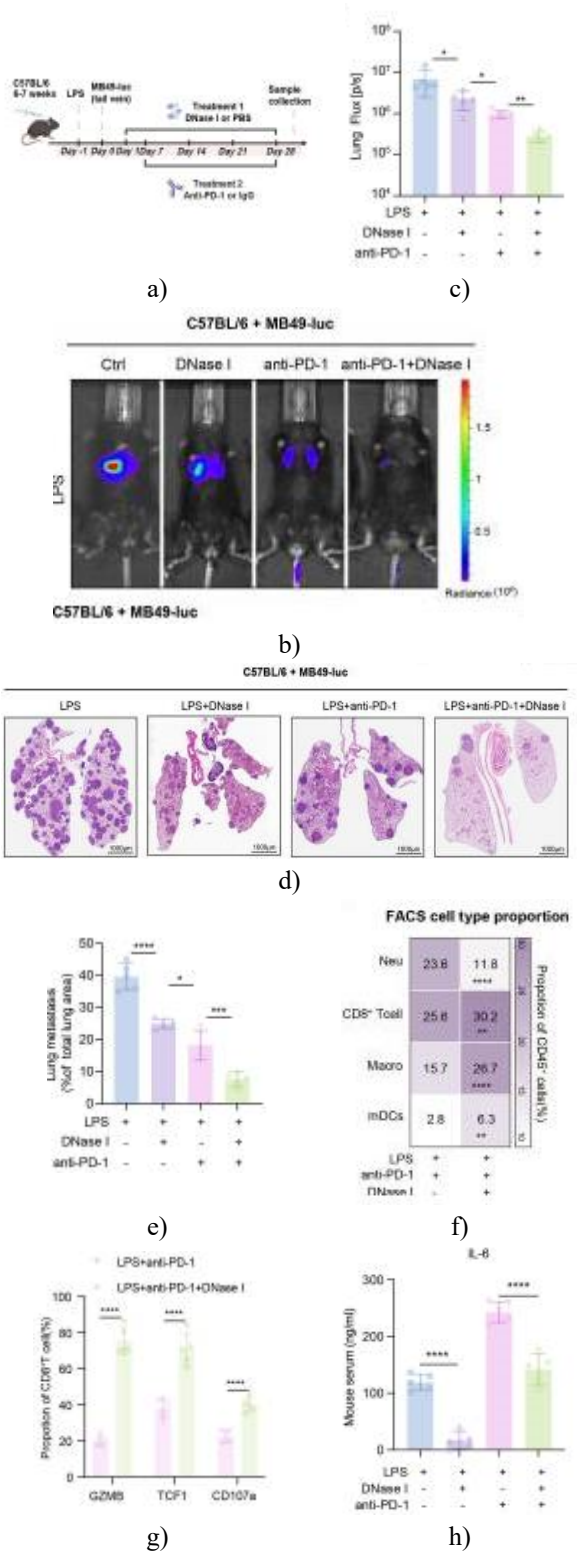

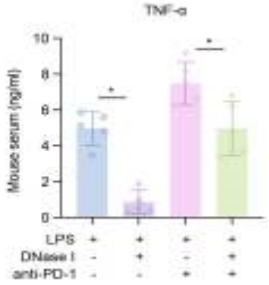

i)

Figure 3. Combined Anti-PD-1 and NET Inhibition Enhances Immunotherapy Efficacy While Reducing Immune-Related Toxicity in Mice. (a) Experimental timeline for the LPS-primed MB49-luc lung metastasis model in C57BL/6 mice, indicating treatment groups: PBS or DNase I, and IgG control or anti-PD-1. (b–c) Representative bioluminescence images (b) and quantitative analysis (c) demonstrate that the combination of anti-PD-1 with DNase I significantly reduced metastatic lung burden compared with either monotherapy. (d–e) Histopathological assessment via H&E staining (d) and quantification of metastatic area (e) confirmed the superior efficacy of the combination therapy in limiting lung metastases. (f–g) Flow cytometry analysis of CD45+ immune cells in lung tissues showed increased infiltration of CD8+ T cells, neutrophils, macrophages, and dendritic cells in the combination group (f). Functional markers of CD8+ T cells, including granzyme B, TCF1, and CD107a, were also elevated under combination therapy (g). (h–i) Serum ELISA measurements indicated that pro-inflammatory cytokines IL-6 (h) and TNF-α (i) were significantly reduced in the combination group compared with anti-PD-1 monotherapy, providing evidence that NETs inhibition mitigates systemic inflammatory responses. Abbreviations: DCs= dendritic cells; FACS= flow cytometry; TCF1= T cell factor 1; GZMB= granzyme B; IL= interleukin; LPS= lipopolysaccharide; Macro= macrophages; NETs= neutrophil extracellular traps; Neu= neutrophils; PBS= phosphate-buffered saline; PD-1= programmed cell death protein-1; TNF= tumor necrosis factor.

To characterize the tumor microenvironment (TME) across treatment groups, FACS analyses were performed. The combination of anti-PD-1 and DNase I markedly increased CD8+ T-cell infiltration and upregulated their functional markers, including granzyme B, TCF1, and CD107a **(Figures 3f and 3g)**. Concurrently, antigen-presenting cells (macrophages and dendritic cells) were more abundant in the combination group **(Figure 3f)**. Levels of immunosuppressive cytokines IL-4 and TGF-β were lowest in this group, suggesting that NET inhibition enhances APC recruitment and reinforces CD8+ T-cell functionality in vivo [29, 30].

Given the clinical relevance of immune-related adverse events (irAEs) [29, 30], safety endpoints were assessed. Anti-PD-1 treatment alone increased serum ALT, AST, creatinine (CREA), and BUN levels, alongside histopathological evidence of mild-to-moderate hepatic and renal inflammation [31, 32]. In contrast, the combination therapy exhibited minimal organ damage. Furthermore, mice in the anti-PD-1 monotherapy group experienced greater body weight loss and higher systemic IL-6 and TNF-α levels compared with the combination group **(Figures 3h and 3i)**.

To investigate the mechanistic link between neutrophils, NETs, and systemic inflammation [30, 33], scRNA-seq data from patients experiencing irAEs were analyzed. Neutrophil clusters were identified using canonical signature markers, revealing elevated NET-associated transcripts (PADI4, CYBB, NCF1, NCF2) in irAE patients, indicating enhanced NET program priming in this context [34, 35]. Collectively, these findings indicate that NET inhibition not only improves anti-PD-1 efficacy but also reduces systemic inflammatory toxicity, positioning NETs as a promising therapeutic target to enhance both efficacy and tolerability of immunotherapy.

NETs induce proteomic remodeling and upregulate STC1 in bladder cancer cells

To explore the molecular mechanisms by which NETs mediate immune evasion, an in vitro co-culture system was established using NET-conditioned medium (NETs-CM) **(Figure 4a)**. Confocal imaging and FACS analyses demonstrated significant uptake of NETs by tumor cells **(Figure 4b)**, confirming direct NET–tumor cell interactions. After 24 hours of co-culture with NETs-CM, tumor cells exhibited pronounced proteomic changes, including increased expression of STC1, MMP9, and VEGFA, which are associated with immune evasion and metastatic potential [36, 37] **(Figure 4c)**. Gene Set Enrichment Analysis further revealed significant downregulation of immune response pathways in NETs-CM-treated tumor cells. These results

suggest that NETs can reprogram tumor cells toward an immune-evasive phenotype.

a)

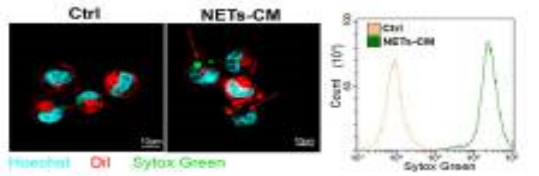

b)

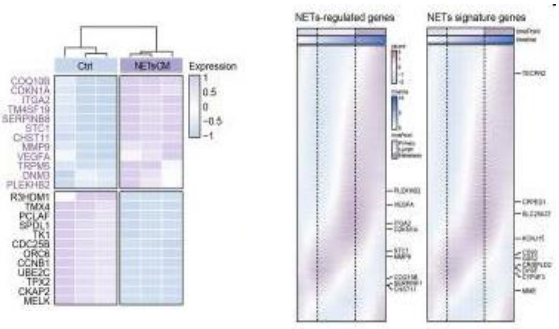

c) d)

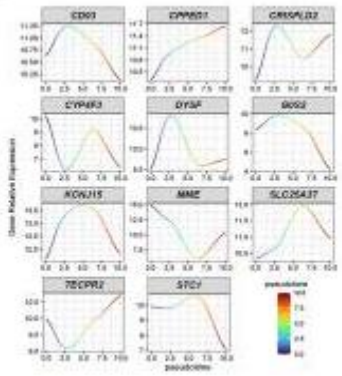

e)

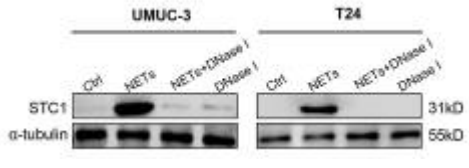

f)

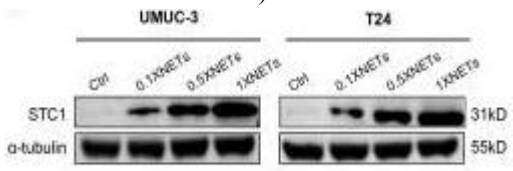

g)

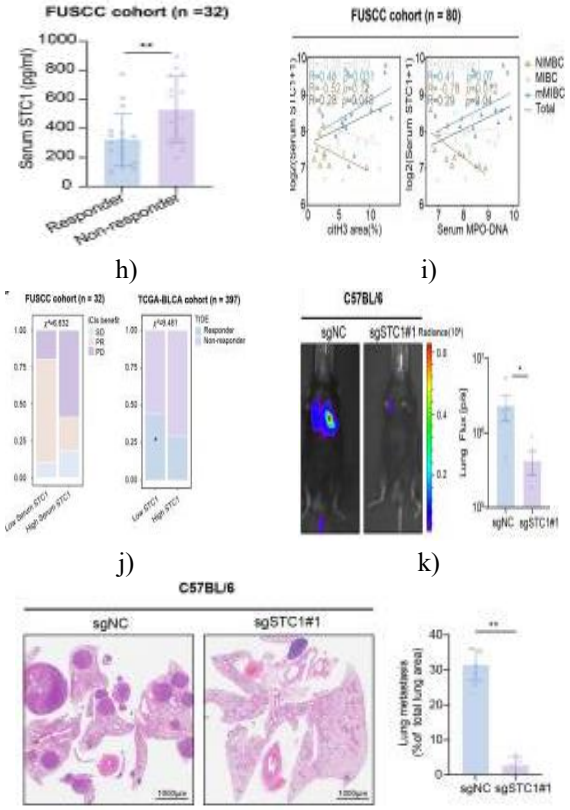

h) i) j) k) l)

Figure 4. NETs Remodel Tumor Proteome and Upregulate the Phagocytosis Checkpoint STC1 in Bladder Cancer. (a) Schematic workflow illustrating the preparation of NET-conditioned medium (NETs-CM) for in vitro experiments. (b) Confocal microscopy and FACS analyses demonstrate the efficient uptake of NETs by bladder cancer cells, confirming direct NET–tumor interactions. (c) Heatmap depicting differential protein expression in tumor cells following NETs-CM treatment, highlighting notable upregulation of STC1, MMP9, and VEGFA. (d–e) Pseudotime trajectory analysis of NET-related genes and STC1 expression in the TCGA-BLCA cohort. Samples were categorized into four groups based on clinicopathological status: primary tumors, lymph node metastases, and distant metastases. Gene expression was averaged within each group, and trajectories inferred from primary tumors to distant metastases revealed sequential upregulation of STC1 followed by NET-associated genes (**Figure 4e**). (f–g) Western blot analyses in UMUC-3 and 5637 cells show STC1 protein induction under NETs-CM treatment, which was reversed by DNase I (f), and a dose-dependent

increase of STC1 with escalating NETs-CM concentrations (g). (h–j) ELISA of serum STC1 in the FUSCC cohort revealed higher levels in immunotherapy non-responders compared with responders (h). STC1 expression positively correlated with tissue citH3 and serum MPO-DNA levels (i), and patients with elevated STC1 exhibited poorer objective response rates to ICIs in both the FUSCC (n=32) and TCGA-BLCA (n=397) cohorts (j). (k–l) Functional in vivo validation: STC1 knockout (sgSTC1) in MB49 cells significantly reduced lung metastases, as shown by bioluminescence imaging (k) and H&E histology with quantification (l).

STC1 functions as a key downstream effector of NETs-mediated immune escape

Among proteins altered by NETs stimulation, STC1 emerged as a critical mediator linked to immune evasion and immunotherapy resistance [38]. STC1 has been described as a pan-cancer phagocytosis checkpoint, upregulated in multiple malignancies and associated with poor prognosis [39, 40]. Pseudotime analysis of bulk TCGA-BLCA data confirmed that STC1 upregulation precedes the activation of NET-related genes **(Figures 4d and 4e)**, supporting its role as a downstream effector of NET-induced immune evasion.

Western blot **(Figure 4f)**, qPCR, and ELISA verified STC1 induction after NETs-CM treatment, which was dose-dependent **(Figure 4g)**. Clinically, serum STC1 levels were higher in immunotherapy non-responders, and STC1 expression increased with tumor progression, peaking in metastatic lesions, mirroring NET dynamics **(Figure 4h)**. STC1 levels positively correlated with NET markers citH3 and MPO-DNA **(Figure 4i)**, and elevated STC1 predicted reduced ICI benefit and poorer survival outcomes **(Figure 4j)**. In vivo, STC1 knockout substantially decreased lung metastasis in C57BL/6 mice **(Figures 4k and 4l)**, demonstrating its central role in NET-driven immune evasion and metastatic progression.

STC1 impairs antigen presentation via APCs

To determine whether STC1-mediated immunosuppression involves APCs, macrophages were depleted in vivo using anti-CSF1R in C57BL/6 mice. In IgG-treated controls, STC1 knockout reduced lung metastases **(Figures 5a and 5b)** and enhanced CD8+ T-cell infiltration and effector function, including IFN-γ and granzyme B production **(Figures 5c and 5d)**. Notably, these STC1-dependent effects were abolished upon APC depletion, indicating that STC1 suppresses CD8+ T-cell immunity through an APC-dependent mechanism.

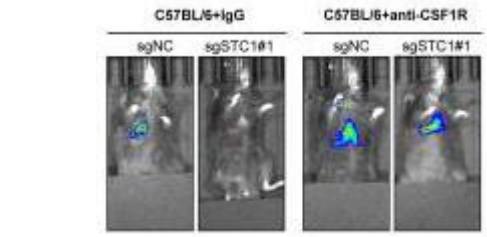

a)

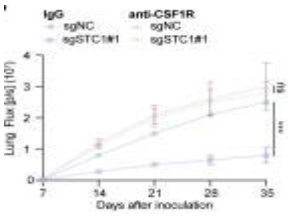

b)

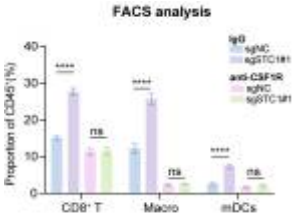

c)

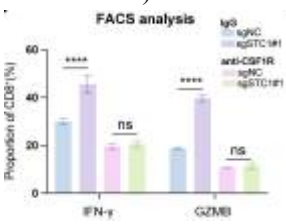

d)

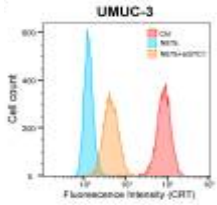

e)

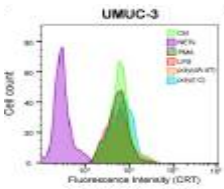

f)

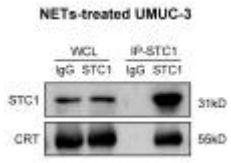

g)

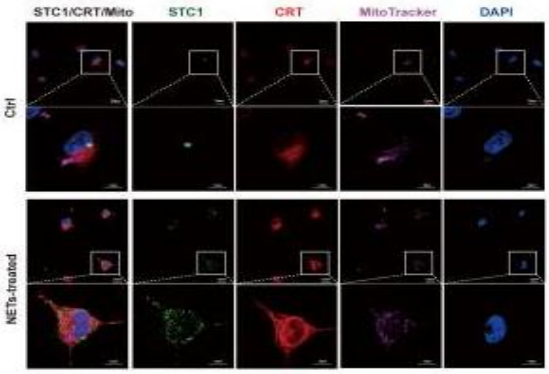

h)

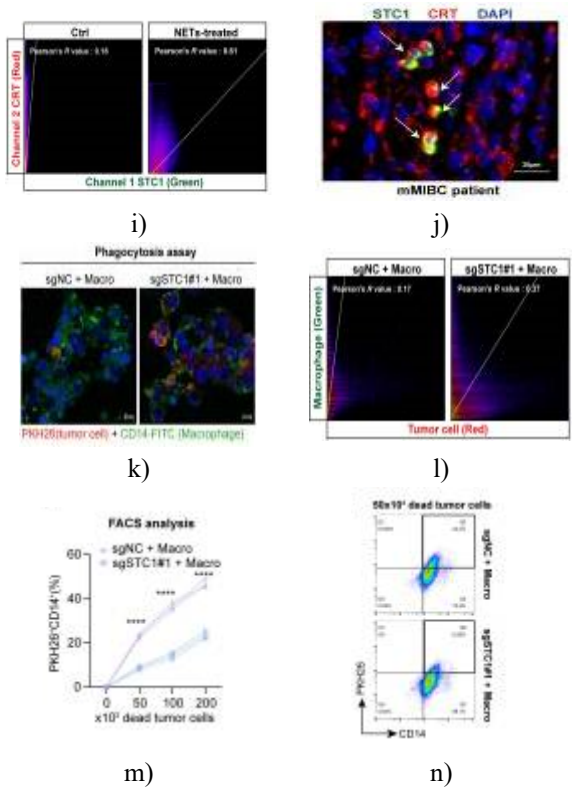

Figure 5. STC1 impedes antigen presentation by trapping CRT in mitochondria. (a–b) In vivo bioluminescence imaging (a) and quantitative radiance analysis of lung metastases (b) in C57BL/6 mice without LPS pre-treatment, comparing sgNC and sgSTC1#1 groups treated with IgG or anti-CSF1R. (c–d) FACS-based profiling of tumor-infiltrating immune cells: (c) proportions of CD8+ T cells, macrophages (Macro), and mature dendritic cells (mDCs) among CD45+ populations; (d) CD8+ T-cell effector activity (IFN-γ, GZMB) under different treatments. (e–f) Flow cytometry quantification of surface CRT under various stimuli (Ctrl, NETs, LPS, PMA, poly(dA:dT), poly(I:C)) and following STC1 knockdown (±siSTC1) in UMUC-3 cells. (g) Co-immunoprecipitation (Co-IP) to detect STC1–CRT interactions in NETs-treated UMUC-3 cells. (h–i) Confocal imaging (h) and quantitative assessment (i) of STC1–CRT co-localization within mitochondria in vitro. (j) Representative IF images of STC1–CRT overlap in tumor tissues from mMIBC patients. (K–N) Phagocytosis assays: (k) confocal images of co-cultures (PKH26-labeled tumor cells in red; CD14+ macrophages in green), (l) Pearson's correlation for co-localization, (m) FACS-based PKH26+CD14+ double-positive percentages across tumor:macrophage ratios, and (n) representative FACS plots for gating double-positive events. Abbreviations: mMIBC= metastatic muscle-invasive bladder cancer; CRT= calreticulin; FACS= flow cytometry; GZMB= granzyme B; IF= immunofluorescence; IFN= interferon; LPS= lipopolysaccharide; Macro= macrophages; mDC, mature dendritic cells; NETs= neutrophil extracellular traps; PMA= phorbol 12-myristate 13-acetate; Co-IP= co-immunoprecipitation.

Antigen-presenting cells (APCs) detect "eat-me" and "don't eat me" signals on tumor surfaces to regulate phagocytosis [41]. CRT functions as a key pro-phagocytic signal [37, 42, 43]. Our experiments revealed that NETs selectively suppressed surface CRT on tumor cells **(Figure 5e)**, a phenomenon not reproduced by LPS, PMA, poly(dA:dT), or poly(I:C) **(Figure 5f)**. Silencing STC1 restored CRT levels on the cell surface, while total CRT abundance remained essentially unchanged **(Figure 5e)**, indicating that NETs impair CRT translocation rather than its synthesis.

To examine whether STC1 physically interacts with CRT, Co-IP assays confirmed a STC1–CRT association in NETs-treated UMUC-3 cells **(Figure 5g)** and HEK293T cells. Confocal imaging demonstrated increased intracellular co-localization of STC1 and CRT specifically in the mitochondrial compartment in vitro **(Figures 5h and 5i)**, which was recapitulated in mMIBC patient tumor tissues **(Figure 5j)**. Dual-IF analyses further showed that STC1–CRT co-localization was higher in NETs-rich (LPS) lesions compared with DNase I-treated lesions. Collectively, these findings suggest a mechanism in which NETs induce STC1, which sequesters CRT in mitochondria, thereby limiting its surface exposure.

Functionally, STC1 depletion enhanced macrophage-mediated phagocytosis in tumor co-cultures **(Figures 5k and 5l)**. FACS analysis corroborated these observations, showing increased PKH26+CD14+ double-positive events at multiple tumor: macrophage ratios **(Figures 5m and 5n)**. Overall, these results reveal a NETs–STC1–CRT axis that diminishes tumor immunogenicity by preventing surface CRT display, reducing macrophage phagocytosis, and suppressing CD8+ T-cell responses.

NETs transcriptionally induce STC1 through the TLR2–MAPK–FosL1 pathway

To elucidate how NETs enhance STC1 expression, we integrated NETs-CM proteomics with TF prediction databases and identified FosL1 as the primary candidate regulating STC1 **(Figure 6a)**. In TCGA BLCA datasets, STC1 expression correlated positively with FosL1 levels **(Figure 6b)**. FosL1 silencing markedly lowered STC1 expression, even under NETs-CM stimulation **(Figure 6c)**. JASPAR analysis predicted a FosL1 binding site in the STC1 promoter **(Figure 6d)**, supported by ChIP-seq peaks in multiple BLCA cell lines **(Figure 6e)**. ChIP-qPCR in UMUC-3 cells validated FosL1 binding to the STC1 promoter, with significant enrichment in the FosL1-IP group relative to IgG controls **(Figures 6f and 6g)**. Dual-luciferase reporter assays confirmed that FosL1 overexpression boosted STC1 promoter activity **(Figure 6h)**. Previous reports indicate MAPK regulates FosL1 [44, 45], and in line with this, NETs activated MAPK–FosL1 signaling, leading to STC1 upregulation **(Figure 6i)**.

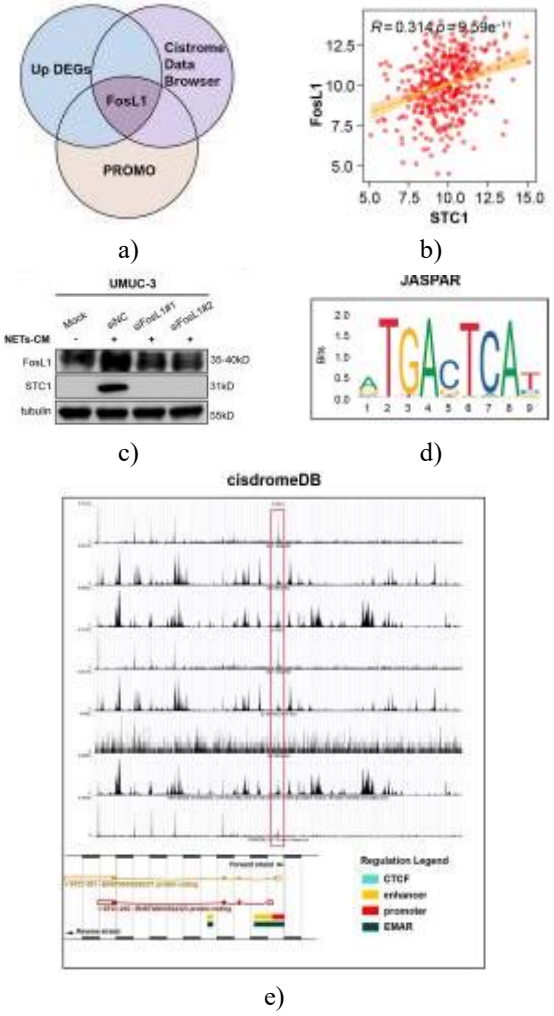

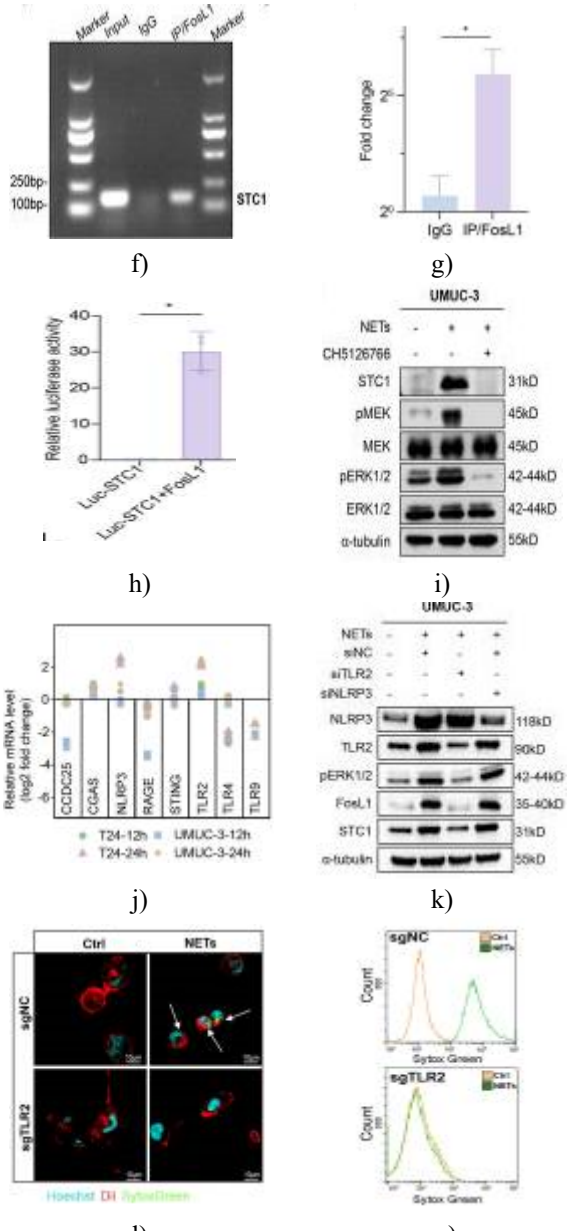

Figure 6. NETs induce STC1 transcription through TLR2–MAPK–FosL1 signaling. (a) A Venn diagram depicting the overlap of transcription factors: those upregulated by NETs-conditioned medium (proteomics), predicted STC1 regulators from the PROMO database, and TFs with ChIP-seq peaks at the STC1 promoter from Cistrome, revealing FosL1 as the common regulator. (b) Correlation between FosL1 and STC1 expression in the TCGA-BLCA cohort. (c) Western blot demonstrating STC1 levels in UMUC-3 cells following FosL1 knockdown using two distinct siRNAs (siFosL1#1, siFosL1#2) under NETs-CM treatment. (d) Predicted FosL1 binding

motif in the STC1 promoter from the JASPAR database. (e) ChIP-seq enrichment of FosL1 at the STC1 promoter across several bladder cancer cell lines (Cistrome Data Browser). (f–g) ChIP-qPCR analysis confirming FosL1 occupancy on the STC1 promoter in UMUC-3 cells relative to IgG controls. (h) Dual-luciferase reporter assay evaluating STC1 promoter activity with or without FosL1 overexpression in HEK293T cells. (i) Western blot showing NETs-induced activation of MAPK and STC1 in UMUC-3 cells, with or without MEK inhibitor CH5126766. (j) qPCR profiling of DAMP-sensing receptors and chromatin/DNA sensors in T24 and UMUC-3 cells after NETs exposure, normalized as indicated. (k) Western blot analysis of MAPK–FosL1–STC1 signaling in cells with receptor perturbations (siNC, siTLR2, siNLRP3) under NETs stimulation. (l–m) Fluorescent imaging of NETs internalization (l) and FACS-based quantification of NET uptake (m) in control (sgNC) and TLR2 knockout cells (sgTLR2). Abbreviations: TCGA= The Cancer Genome Atlas; BLCA= bladder cancer; ChIP-seq= chromatin immunoprecipitation sequencing; CM= conditioned medium; FACS= flow cytometry; NETs= neutrophil extracellular traps; qPCR= quantitative PCR.

To decipher how bladder cancer cells sense and internalize NETs to trigger STC1 transcription, we interrogated classical DAMP-sensing pathways, including cGAS–STING, multiple TLRs (TLR2, TLR4, TLR9), NLRP3, CCDC25, and RAGE [22, 46, 47]. NETs selectively enhanced TLR2 and NLRP3 mRNA in UMUC-3 and T24 cells, whereas other pathways, including cGAS–STING, CCDC25, RAGE, and other TLRs, showed minimal changes **(Figure 6j)**. Functionally, silencing TLR2 (siTLR2) blunted NETs-induced MAPK phosphorylation, reduced FosL1 expression, and suppressed STC1 upregulation, while knockdown of NLRP3 had no discernible effect **(Figure 6k)**. Additionally, deletion of TLR2 significantly impaired NETs internalization in UMUC-3 cells **(Figures 6l and 6m)**. These findings reveal a TLR2-to-promoter cascade whereby NETs engagement of TLR2 activates the MAPK–FosL1 axis, driving STC1 transcription in bladder cancer cells.

Given that STC1 is secreted, we next explored its paracrine effects within the tumor microenvironment. ELISA measurements confirmed substantial accumulation of STC1 in the extracellular milieu **(Figure 4h)**. To test whether secreted STC1 promotes NETs formation, we generated STC1 knockdown lines and collected their conditioned medium to stimulate neutrophils in vitro. Neutrophils exposed to CM from STC1-high cells formed abundant NETs, as revealed by immunofluorescence, whereas CM from STC1-low or knockout cells led to markedly reduced NET formation **(Figures 7a and 7b)**.

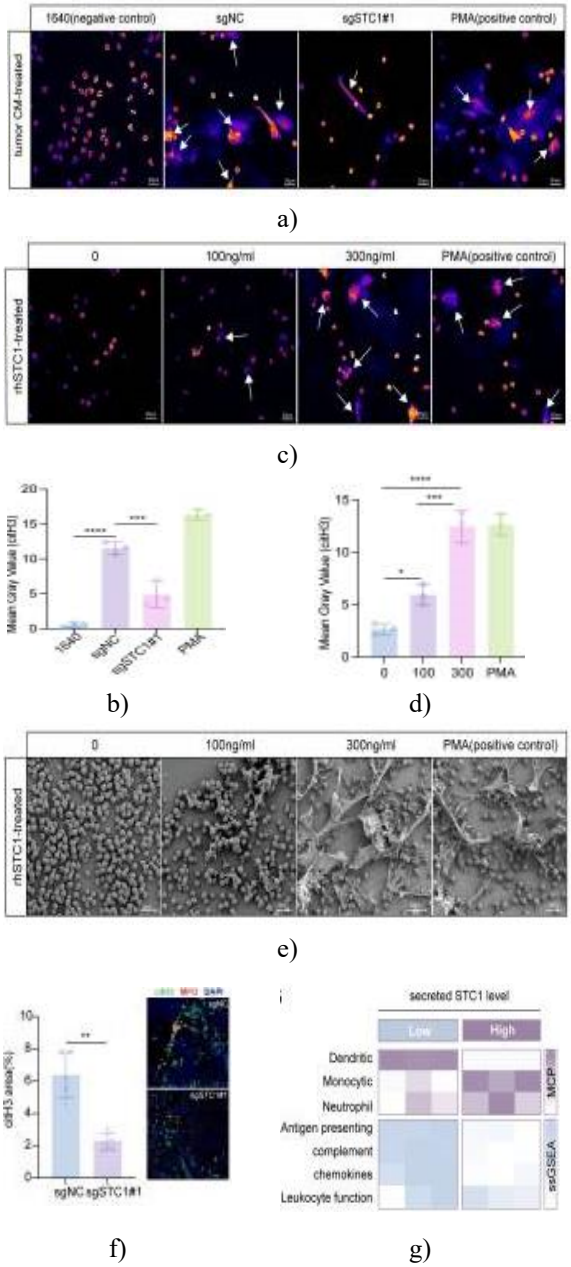

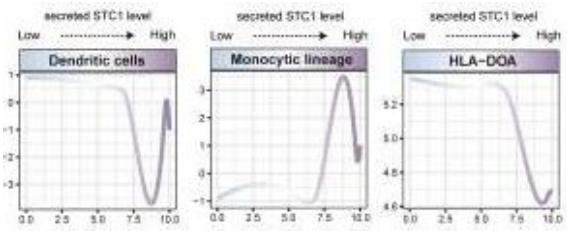

h)

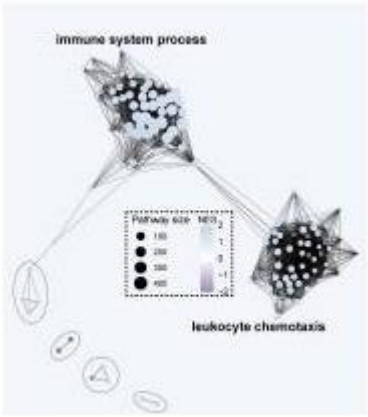

i)

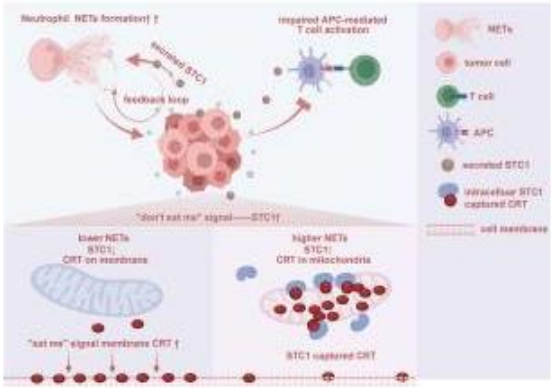

j)

Figure 7. Secreted STC1 drives NETs formation and disrupts APC maturation, establishing a self-reinforcing immunosuppressive loop. (a–b) Representative immunofluorescence images of neutrophils stained for citH3, MPO, and DAPI following incubation with conditioned medium (CM) from sgNC or sgSTC1#1 tumor cells, with quantitative analysis of citH3 mean gray intensity (b). PMA and RPMI-1640 served as positive and negative controls, respectively. (c–d) Dose-dependent induction of NETs in neutrophils treated with recombinant human STC1 (rhSTC1), visualized by IF (c) and quantified by citH3 mean gray value (d). (e) SEM images illustrating NETs morphology under low and high STC1 CM conditions, alongside control groups. (f) IF analysis of lung metastatic lesions from mice bearing sgSTC1 or sgNC tumors, staining for citH3/MPO/DAPI, with quantification of citH3-positive area. (g) MCP-counter and ssGSEA analysis of RNA-seq data from CD14+ monocytes co-cultured with STC1 knockdown or control tumor cells. (h) Pseudotime trajectories depicting dendritic cell differentiation, monocyte lineage progression, and HLA-DOA expression between low and high STC1 groups. (i) Enrichment network highlighting activated biological pathways (NES>0) in low STC1 conditions, with major differences annotated. (j) Graphic abstract summarizing study findings. Abbreviations: DAPI= 4′,6-diamidino-2-phenylindole; MCP= Microenvironment Cell Populations; RPMI= Roswell Park Memorial Institute; APC= antigen-presenting cell; CM= conditioned medium; CRT= calreticulin; IF= immunofluorescence; MPO= myeloperoxidase; NETs, neutrophil extracellular traps; PMA, phorbol 12-myristate 13-acetate; rhSTC1= recombinant human STC1; RNA-seq= RNA sequencing; SEM= scanning electron microscopy; ssGSEA= single-sample Gene Set Enrichment Analysis.

In vivo examination revealed that NETs were scarcely detectable in lung metastases derived from sgSTC1 tumors, whereas sgNC lesions displayed abundant NETs structures **(Figure 7f)**. To determine whether STC1 alone can drive NETs formation, neutrophils were treated with escalating doses of rhSTC1. NETs formation increased in a dose-dependent manner, with 300 ng/mL producing pronounced web-like structures **(Figure 7e)**. RNA-seq profiling of sgNC and sgSTC1 tumor cells demonstrated that canonical NETosis-inducing factors—including PGE2 (Ptges, Ptgs2), MIF (Mif), TGF-β1 (Tgfb1), TNF-α (Tnf), IL-1β (Il1b), GM-CSF (Csf2), G-CSF (Csf3), cathepsins B/L (Ctsb, Ctsl), and HMGB1 (Hmgb1) [27, 28, 35]—were not significantly altered. Collectively, these results indicate that secreted STC1 is sufficient to trigger NETs, forming a positive feedback loop in the tumor microenvironment that can amplify immunosuppression and metastatic progression.

Beyond NETs induction, we investigated the impact of secreted STC1 on APC differentiation. CD14+ monocytes were co-cultured with either STC1 knockdown or control tumor cells and analyzed by RNA-seq. MCP-counter and ssGSEA revealed that monocytes exposed to low STC1 conditions exhibited enhanced

antigen-presenting capacity **(Figure 7g)**. Pseudotime analysis showed that reduced STC1 favored differentiation toward dendritic cells while limiting monocyte and neutrophil proportions **(Figure 7h)**. Key immunosuppressive genes, including IL1RN, CSF1, and S100A9, were downregulated under low STC1 conditions, whereas immune-activating chemokines such as CXCL9, CXCL10, and antigen-presentation molecule HLA-DOA were upregulated Functional enrichment analysis indicated that genes upregulated in low STC1 conditions were enriched in immune activation and leukocyte chemotaxis pathways, whereas high STC1 conditions preferentially enhanced granulocyte chemotaxis, potentially promoting neutrophil infiltration **(Figure 7i)**. These findings demonstrate that secreted STC1 not only facilitates NETs formation but also transcriptionally reprograms CD14+ APC precursors, further suppressing antitumor immunity.

The study's graphic abstract **(Figure 7j)** integrates these findings: NETs accumulation in bladder cancer triggers immune evasion through STC1. NETs stimulate STC1 expression via TLR2–MAPK–FosL1, suppressing antigen presentation by capturing CRT. Extracellular STC1 amplifies NETs formation, creating a self-reinforcing immunosuppressive loop, while also reprogramming APC precursors to diminish antitumor immunity.

In conclusion, these results identify a NETs–STC1 positive feedback loop as a central mechanism mediating immune evasion in bladder cancer, highlighting a potential therapeutic axis for restoring antitumor immunity and enhancing immunotherapy efficacy.

Despite the remarkable progress of immunotherapy in bladder cancer (BLCA), clinical outcomes remain limited due to high rates of therapeutic resistance and the relatively small proportion of patients who benefit [4, 7, 48]. Recently, there has been growing interest in the immunosuppressive roles of innate immune components within the tumor microenvironment (TME), particularly tumor-associated neutrophils (TANs) and their release of neutrophil extracellular traps (NETs) [20]. While NETs were originally recognized as a defense mechanism against pathogens, accumulating evidence indicates that they can promote metastasis and thrombosis in various solid tumors [49, 50]. Several TME factors—including inflammatory cytokines, damage-associated molecular patterns (DAMPs), and tumor-derived chemokines [28]—have been implicated in NET accumulation. However, their contribution to immune evasion and tumor progression in BLCA remains poorly understood, as most prior studies have focused on NETs' physical barrier effects or their role in epithelial-mesenchymal transition (EMT), with limited exploration of their immunoregulatory interactions with tumor cells.

In the present study, we investigated the role of NETs in mediating immune resistance in BLCA through a multi-level approach, spanning clinical observations to mechanistic validation. Analysis of two real-world BLCA immunotherapy cohorts revealed that NET levels were markedly higher in patients who did not respond to therapy. In vivo, NETs promoted metastasis in an immune-dependent manner, whereas NET targeting enhanced the efficacy of immune checkpoint inhibitors (ICIs) and reduced immune-related adverse effects. Mechanistically, NETs activated the TLR2–MAPK–FosL1 signaling axis, driving transcriptional upregulation of the phagocytic checkpoint STC1 and facilitating immune evasion. Moreover, STC1 exerted dual functions: intracellular STC1 impeded CRT-mediated antigen presentation and phagocytosis, while secreted STC1 promoted aberrant NET formation, creating a self-reinforcing loop that intensified immunosuppression and disrupted the maturation of APC precursors. This cascade offers a mechanistic rationale for optimizing combination therapies in BLCA.

NETs, as critical effector products of neutrophils, have long been recognized for their role in host defense [20, 27]. However, mounting evidence indicates that chronic NET-mediated inflammation can facilitate tumor progression [28]. NETs can form physical barriers that shield tumor cells from T cell-mediated cytotoxicity [51] or promote EMT [22, 52]. Our findings extend this understanding by revealing that NETs also contribute to immune escape through modulation of tumor-intrinsic anti-phagocytic pathways. This mechanism operates alongside adaptive immune suppression—such as T cell exhaustion and immune checkpoint inhibition [53, 54]—highlighting a previously underappreciated molecular crosstalk between innate immune cells and tumor-driven immune evasion strategies.

Our study identifies STC1 as a central mediator of NETs-induced immune evasion in bladder cancer (BLCA). STC1, a recently characterized innate immune checkpoint molecule validated across over 20 cancer types, plays a pivotal role in regulating tumor cell phagocytosis. Effective antitumor immunity depends on a tightly regulated balance between pro-phagocytic signals, such as calreticulin (CRT), and anti-phagocytic

checkpoints, including STC1 and CD47, on the tumor cell surface [48, 50]. Membrane-exposed CRT functions as an “eat me” signal, promoting recognition and clearance of tumor cells by antigen-presenting cells (APCs). Tumor cells, however, can hijack this system by upregulating anti-phagocytic molecules, thereby circumventing CRT-mediated detection. In our study, we confirmed a novel function of STC1 in sequestering CRT intracellularly, thereby inhibiting antigen presentation. This reinforces the concept that the imbalance between pro- and anti-phagocytic signals is a key driver of BLCA progression and contributes to differential responses to immunotherapy.

Beyond its intracellular effects, the role of secreted STC1 has been largely unexplored. Unexpectedly, we found that extracellular STC1 enhances NET formation, creating a self-reinforcing feedback loop that further strengthens immune evasion. This mechanism may partially explain the complex and refractory nature of immunotherapy resistance in BLCA, suggesting that monotherapy is often insufficient to overcome an established immune-suppressive TME. These findings underscore the potential value of combination therapeutic strategies targeting both STC1 and NETs.

Clinically, our observations are consistent with adverse events seen during anti-PD-1 therapy. Patients frequently exhibited elevated serum markers—ALT, AST, CREA, and BUN—alongside acute inflammatory histopathology in the liver and kidneys, highlighting the challenge of immune-related adverse events (irAEs) [55]. Mechanistically, we observed a potential link between NET formation and irAEs [33]. Neutrophils from patients experiencing irAEs showed upregulation of NET-associated transcripts, consistent with prior evidence linking NETs to autoimmunity [27], endothelial injury [56], and amplification of cytokine cascades [57]. Importantly, NET inhibition mitigated organ damage and inflammation induced by anti-PD-1 therapy without compromising its antitumor efficacy. These results suggest that NETs play a previously underappreciated role in ICIs-related toxicity and that targeting NETs could simultaneously improve therapeutic safety and efficacy. Nonetheless, several limitations should be noted: (1) transcript abundance in neutrophils does not directly measure NETosis; (2) circulating cytokine levels (IL-6, TNF-α) are not exclusive markers of NET activity; and (3) cohort size, sampling windows, and heterogeneity in treatment regimens may introduce confounding factors, including infections, antibiotic exposure, or subclinical tissue injury.

While NET-targeting strategies show promise, potential risks remain. NETs are critical for host defense against pathogens, and broad inhibition could impair systemic immunity and increase susceptibility to infection. Future approaches should aim to selectively modulate tumor-associated NETs while preserving overall innate immune function. Additionally, the drivers of excessive NET accumulation in BLCA remain to be fully elucidated. It is unclear whether this is primarily due to increased NET production, impaired degradation, or both, and the contributions of TME components—cytokines, DAMPs, or tumor-derived factors—require further investigation. Resolving these questions will facilitate safer and more controlled therapeutic targeting of the NETs–STC1 axis in clinical settings.

Conclusion

In summary, our study delineates a critical immunosuppressive feedback loop in BLCA, orchestrated by NETs and STC1. NETs induce upregulation of the phagocytic checkpoint STC1 via the TLR2–MAPK–FosL1 pathway, while STC1 reciprocally promotes NET formation, establishing a self-amplifying cycle that impairs antigen presentation and drives immune escape. Disrupting this loop through inhibition of NETs or STC1 restores APC function and enhances immunotherapy efficacy. Furthermore, NETs contribute to irAEs, and their modulation offers the dual benefit of reducing inflammatory toxicity while preserving antitumor activity. These findings highlight the central role of the NETs–STC1 circuit in immune resistance and therapy-related toxicity, providing a strong rationale for combinatorial strategies to improve both the safety and effectiveness of immunotherapy in BLCA.

Acknowledgments: None

Conflict of Interest: None

Financial Support: This work was supported by grants from the National Natural Science Foundation of China (No. 82473192, 82172741), Shanghai Municipal Health Bureau (No.2020CXJQ03), Scientific Innovation Project of Shanghai Education Committee (No.2021-01-07-00-07-E00080). We acknowledge BioRender.com for providing icons of illustrations

Ethics Statement: Ethics approval and consent to participate. Clinical sample collection in this study was approved by the Institutional Review Board of FUSCC (Approval No.: 050432-4-2307E) and SYSUCC (Approval No.: G2024-056-01). All conducted in accordance with the ethical principles outlined in the Declaration of Helsinki. Written informed consent was obtained from all participants. Animal experiments in this study were conducted in accordance with the guidelines of the Animal Ethics Committee of FUSCC (Approval No.: FUSCC-IACUC-S2025-0460).

References

1. Han B, Zheng R, Zeng H, et al. Cancer incidence and mortality in China, 2022. J Natl Cancer Cent . 2024;4:47–53. doi: 10.1016/j.jncc.2024.01.006.
2. Alfred Witjes J, Max Bruins H, Carrión A, et al. European Association of Urology Guidelines on Muscle-invasive and Metastatic Bladder Cancer: Summary of the 2023 Guidelines. Eur Urol. 2024;85:17–31. doi: 10.1016/j.eururo.2023.08.016.
3. Fan X. Recent highlights of cancer immunotherapy. Holist Integ Oncol . 2023;2:37. doi: 10.1007/s44178-023-00057-6.
4. Spaas M, Sundahl N, Kruse V, et al. Checkpoint Inhibitors in Combination With Stereotactic Body Radiotherapy in Patients With Advanced Solid Tumors: The CHEERS Phase 2 Randomized Clinical Trial. JAMA Oncol. 2023;9:1205–13. doi: 10.1001/jamaoncol.2023.2132.
5. Lopez-Beltran A, Cookson MS, Guercio BJ, et al. Advances in diagnosis and treatment of bladder cancer. BMJ. 2024;384:e076743. doi: 10.1136/bmj-2023-076743.
6. Nadal R, Valderrama BP, Bellmunt J. Progress in systemic therapy for advanced-stage urothelial carcinoma. Nat Rev Clin Oncol. 2024;21:8–27. doi: 10.1038/s41571-023-00826-2.
7. Balar AV, Castellano DE, Grivas P, et al. Efficacy and safety of pembrolizumab in metastatic urothelial carcinoma: results from KEYNOTE-045 and KEYNOTE-052 after up to 5 years of follow-up. Ann Oncol. 2023;34:289–99. doi: 10.1016/j.annonc.2022.11.012.
8. Holder AM, Dedeilia A, Sierra-Davidson K, et al. Defining clinically useful biomarkers of immune checkpoint inhibitors in solid tumours. Nat Rev Cancer. 2024;24:498–512. doi: 10.1038/s41568-024-00705-7.
9. Khosravi G-R, Mostafavi S, Bastan S, et al. Immunologic tumor microenvironment modulators for turning cold tumors hot. Cancer Commun (Lond) 2024;44:521–53. doi: 10.1002/cac2.12539.
10. Guo CC, Lee S, Lee JG, et al. Molecular profile of bladder cancer progression to clinically aggressive subtypes. Nat Rev Urol. 2024;21:391–405. doi: 10.1038/s41585-023-00847-7.
11. Ouyang Y, Ou Z, Zhong W, et al. FGFR3 Alterations in Bladder Cancer Stimulate Serine Synthesis to Induce Immune-Inert Macrophages That Suppress T-cell Recruitment and Activation. Cancer Res. 2023;83:4030–46. doi: 10.1158/0008-5472.CAN-23-1065.
12. Sadhukhan P, Feng M, Illingworth E, et al. YAP1 induces bladder cancer progression and promotes immune evasion through IL-6/STAT3 pathway and CXCL deregulation. J Clin Invest. 2024;135:e171164. doi: 10.1172/JCI171164.
13. Oh DY, Kwek SS, Raju SS, et al. Intratumoral CD4+ T Cells Mediate Anti-tumor Cytotoxicity in Human Bladder Cancer. Cell. 2020;181:1612–25. doi: 10.1016/j.cell.2020.05.017.
14. Yoshida GJ. Regulation of heterogeneous cancer-associated fibroblasts: the molecular pathology of activated signaling pathways. J Exp Clin Cancer Res. 2020;39:112. doi: 10.1186/s13046-020-01611-0.
15. Lei A, Yu H, Lu S, et al. A second-generation M1-polarized CAR macrophage with antitumor efficacy. Nat Immunol. 2024;25:102–16. doi: 10.1038/s41590-023-01687-8.
16. Shinde-Jadhav S, Mansure JJ, Rayes RF, et al. Role of neutrophil extracellular traps in radiation resistance of invasive bladder cancer. Nat Commun. 2021;12:2776. doi: 10.1038/s41467-021-23086-z.
17. Xie P, Yu M, Zhang B, et al. CRKL dictates anti-PD-1 resistance by mediating tumor-associated neutrophil infiltration in hepatocellular carcinoma. J Hepatol. 2024;81:93–107. doi: 10.1016/j.jhep.2024.02.009.
18. Sui Q, Zhang X, Chen C, et al. Inflammation promotes resistance to immune checkpoint inhibitors in high microsatellite instability colorectal cancer. Nat Commun. 2022;13:7316. doi: 10.1038/s41467-022-35096-6.

19. Jaillon S, Ponzetta A, Di Mitri D, et al. Neutrophil diversity and plasticity in tumour progression and therapy. Nat Rev Cancer. 2020;20:485–503. doi: 10.1038/s41568-020-0281-y.
20. Maiorino L, Daßler-Plenker J, Sun L, et al. Innate Immunity and Cancer Pathophysiology. Annu Rev Pathol. 2022;17:425–57. doi: 10.1146/annurev-pathmechdis-032221-115501.
21. Poli V, Zanoni I. Neutrophil intrinsic and extrinsic regulation of NETosis in health and disease. Trends Microbiol. 2023;31:280–93. doi: 10.1016/j.tim.2022.10.002.
22. Yang L, Liu Q, Zhang X, et al. DNA of neutrophil extracellular traps promotes cancer metastasis via CCDC25. Nature New Biol. 2020;583:133–8. doi: 10.1038/s41586-020-2394-6.
23. MacDonald KPA, Palmer JS, Cronau S, et al. An antibody against the colony-stimulating factor 1 receptor depletes the resident subset of monocytes and tissue- and tumor-associated macrophages but does not inhibit inflammation. Blood. 2010;116:3955–63. doi: 10.1182/blood-2010-02-266296.
24. Zhu H, Galdos FX, Lee D, et al. Identification of Pathogenic Immune Cell Subsets Associated With Checkpoint Inhibitor–Induced Myocarditis. Circulation. 2022;146:316–35. doi: 10.1161/CIRCULATIONAHA.121.056730.
25. Becht E, Giraldo NA, Lacroix L, et al. Estimating the population abundance of tissue-infiltrating immune and stromal cell populations using gene expression. Genome Biol. 2016;17:218. doi: 10.1186/s13059-016-1070-5.
26. Meng J, Zhou Y, Lu X, et al. Immune response drives outcomes in prostate cancer: implications for immunotherapy. Mol Oncol. 2021;15:1358–75. doi: 10.1002/1878-0261.12887.
27. Papayannopoulos V. Neutrophil extracellular traps in immunity and disease. Nat Rev Immunol. 2018;18:134–47. doi: 10.1038/nri.2017.105.
28. Adrover JM, McDowell SAC, He X-Y, et al. NETworking with cancer: The bidirectional interplay between cancer and neutrophil extracellular traps. Cancer Cell. 2023;41:505–26. doi: 10.1016/j.ccell.2023.02.001.
29. Müller-Jensen L, Schulz AR, Mei HE, et al. Immune signatures of checkpoint inhibitor-induced autoimmunity-A focus on neurotoxicity. Neuro Oncol . 2024;26:279–94. doi: 10.1093/neuonc/noad198.
30. Zhou Y, Medik YB, Patel B, et al. Intestinal toxicity to CTLA-4 blockade driven by IL-6 and myeloid infiltration. J Exp Med. 2023;220:e20221333. doi: 10.1084/jem.20221333.
31. Seethapathy H, Herrmann SM, Sise ME. Immune Checkpoint Inhibitors and Kidney Toxicity: Advances in Diagnosis and Management. Kidney Med . 2021;3:1074–81. doi: 10.1016/j.xkme.2021.08.008.
32. De Martin E, Michot J-M, Papouin B, et al. Characterization of liver injury induced by cancer immunotherapy using immune checkpoint inhibitors. J Hepatol. 2018;68:1181–90. doi: 10.1016/j.jhep.2018.01.033.
33. Guo J, Shu T, Zhang H, et al. A combined model of serum neutrophil extracellular traps, CD8+ T cells, and tumor proportion score provides better prediction of PD-1 inhibitor efficacy in patients with NSCLC. FEBS J. 2024;291:3403–16. doi: 10.1111/febs.17144.
34. Kenny EF, Herzig A, Krüger R, et al. Diverse stimuli engage different neutrophil extracellular trap pathways. Elife. 2017;6:e24437. doi: 10.7554/eLife.24437.
35. de Bont CM, Boelens WC, Pruijn GJM. NETosis, complement, and coagulation: a triangular relationship. Cell Mol Immunol. 2019;16:19–27. doi: 10.1038/s41423-018-0024-0.
36. Pérez-Gutiérrez L, Ferrara N. Biology and therapeutic targeting of vascular endothelial growth factor A. Nat Rev Mol Cell Biol. 2023;24:816–34. doi: 10.1038/s41580-023-00631-w.
37. Liu Y, Wang Y, Yang Y, et al. Emerging phagocytosis checkpoints in cancer immunotherapy. Sig Transduct Target Ther. 2023;8:104. doi: 10.1038/s41392-023-01365-z.
38. Cai S. Stanniocalcin-1 relates to tumor recurrence and unfavorable prognosis of urothelial bladder cancer
39. Lin H, Kryczek I, Li S, et al. Stanniocalcin 1 is a phagocytosis checkpoint driving tumor immune resistance. Cancer Cell. 2021;39:480–93. doi: 10.1016/j.ccell.2020.12.023.
40. Feng M, Jiang W, Kim BYS, et al. Phagocytosis checkpoints as new targets for cancer immunotherapy. Nat Rev Cancer. 2019;19:568–86. doi: 10.1038/s41568-019-0183-z.

41. Yang K, Halima A, Chan TA. Antigen presentation in cancer - mechanisms and clinical implications for immunotherapy. Nat Rev Clin Oncol. 2023;20:604–23. doi: 10.1038/s41571-023-00789-4.
42. Fucikova J, Spisek R, Kroemer G, et al. Calreticulin and cancer. Cell Res. 2021;31:5–16. doi: 10.1038/s41422-020-0383-9.
43. Chao MP, Jaiswal S, Weissman-Tsukamoto R, et al. Calreticulin is the dominant pro-phagocytic signal on multiple human cancers and is counterbalanced by CD47. Sci Transl Med. 2010;2:63ra94. doi: 10.1126/scitranslmed.3001375.
44. Wang C, Li Z, Shao F, et al. High expression of Collagen Triple Helix Repeat Containing 1 (CTHRC1) facilitates progression of oesophageal squamous cell carcinoma through MAPK/MEK/ERK/FRA-1 activation. J Exp Clin Cancer Res. 2017;36:84. doi: 10.1186/s13046-017-0555-8.
45. Maurus K, Hufnagel A, Geiger F, et al. The AP-1 transcription factor FOSL1 causes melanocyte reprogramming and transformation. Oncogene. 2017;36:5110–21. doi: 10.1038/onc.2017.135.
46. Ning Y, Chen Y, Tian T, et al. S100A7 orchestrates neutrophil chemotaxis and drives neutrophil extracellular traps (NETs) formation to facilitate lymph node metastasis in cervical cancer patients. Cancer Lett. 2024;605:217288. doi: 10.1016/j.canlet.2024.217288.
47. Zhang Q, Liu S, Wang H, et al. ETV4 Mediated Tumor-Associated Neutrophil Infiltration Facilitates Lymphangiogenesis and Lymphatic Metastasis of Bladder Cancer. Adv Sci (Weinh) 2023;10:e2205613. doi: 10.1002/advs.202205613.
48. Powles T, Valderrama BP, Gupta S, et al. Enfortumab Vedotin and Pembrolizumab in Untreated Advanced Urothelial Cancer. N Engl J Med. 2024;390:875–88. doi: 10.1056/NEJMoa2312117.
49. Mousset A, Lecorgne E, Bourget I, et al. Neutrophil extracellular traps formed during chemotherapy confer treatment resistance via TGF-β activation. Cancer Cell. 2023;41:757–75. doi: 10.1016/j.ccell.2023.03.008.
50. He X-Y, Gao Y, Ng D, et al. Chronic stress increases metastasis via neutrophil-mediated changes to the microenvironment. Cancer Cell. 2024;42:474–86. doi: 10.1016/j.ccell.2024.01.013.
51. Taifour T, Attalla SS, Zuo D, et al. The tumor-derived cytokine Chi3l1 induces neutrophil extracellular traps that promote T cell exclusion in triple-negative breast cancer. Immunity. 2023;56:2755–72. doi: 10.1016/j.immuni.2023.11.002.
52. Zhan X, Wu R, Kong X-H, et al. Elevated neutrophil extracellular traps by HBV-mediated S100A9-TLR4/RAGE-ROS cascade facilitate the growth and metastasis of hepatocellular carcinoma. Cancer Commun (Lond) 2023;43:225–45. doi: 10.1002/cac2.12388.
53. Galassi C, Chan TA, Vitale I, et al. The hallmarks of cancer immune evasion. Cancer Cell. 2024;42:1825–63. doi: 10.1016/j.ccell.2024.09.010.
54. Gebhardt T, Park SL, Parish IA. Stem-like exhausted and memory CD8+ T cells in cancer. Nat Rev Cancer. 2023;23:780–98. doi: 10.1038/s41568-023-00615-0.
55. Tsukamoto H, Komohara Y, Tomita Y, et al. Aging-associated and CD4 T-cell-dependent ectopic CXCL13 activation predisposes to anti-PD-1 therapy-induced adverse events. Proc Natl Acad Sci U S A. 2022;119:e2205378119. doi: 10.1073/pnas.2205378119.
56. Zhang H, Wang Y, Qu M, et al. Neutrophil, neutrophil extracellular traps and endothelial cell dysfunction in sepsis. Clin Transl Med. 2023;13:e1170. doi: 10.1002/ctm2.1170.
57. Zhang H, Wu D, Wang Y, et al. Ferritin-mediated neutrophil extracellular traps formation and cytokine storm via macrophage scavenger receptor in sepsis-associated lung injury. Cell Commun Signal. 2024;22:97. doi: 10.1186/s12964-023-01440-6.